Influence of the position and size of various deterministic defects on the high cycle fatigue resistance of a 316L steel manufactured by laser powder bed fusion

Olivier Andreau[1, 2] Etienne Pessard[3], Imade Koutiri[2], Patrice Peyre[2], Nicolas Saintier[4]

[1]CEA Saclay DIGITEO Labs Bât. 565 91191 Gif-Sur-Yvette Cedex, France

[2]Arts et Metiers Institute of Technology, CNRS, CNAM, PIMM, HESAM Université, F-75013 Paris, France

[3]Arts et Metiers Institute of Technology, LAMPA, HESAM Université, F-49035 Angers, France

[4]Arts et Metiers Institute of Technology, Université de Bordeaux, CNRS, INRA, INP, I2M, HESAMUniversité, F-33400 Talence, France

Abstract

Optimized 316L steel samples were manufactured using laser powder bed fusion and tested in high cycle fatigue at R=0.1. They showed microstructural crack initiation and outstanding fatigue properties. Additional fatigue testings were then carried out on samples containing deterministic defects of various sizes and positions. All results summarized in a Kitagawa-Takahashi diagram show that the critical defect size is around 20 µm for surface defects and reach 380 µm for internal pores. Fracture surface analysis revealed that the large size gap between surface and internal fatigue crack initiation could be linked to the local gaseous environment in the pores.

Keywords: Laser Powder Bed Fusion; Austenitic stainless steel; Fatigue; Defect; Porosity

Corresponding author: Olivier Andreau andreau.olivier@gmail.com +33 647 70 26 87

1. Introduction:

Among the metal additive manufacturing techniques, Laser Powder Bed Fusion (LPBF) is widely recognized as one of the most promising method for the industry of the future, due to the attractive characteristics of built parts including: a high degree of complexity, a good spatial resolution (around 0.1 mm precision), and good mechanical resistance under static loading [1]. In addition, the growing understanding of the link between process parameters and microstructures open the field of microstructure engineering, allowing, for example, the control of local textures or grain sizes [2,3]. For this reason, the range of applications is continuously growing up on a large range of materials, including recently complex metals to process with lasers like pure copper [4].

However, it is also well known that the fabricated parts without post processing are likely to contain defects including: a high roughness, internal pores due to lacks-of-fusion or occluded gas [5], and possible hot-cracking phenomena for instance on a range of nickel-based superalloys [6] or aluminium alloys. Such defects, and especially those promoting stress raisers like surface roughness and pores can promote early fatigue crack initiations and severely affect the material's resistance under cyclic loading [7]. For this reason, as-built 316L LPBF samples usually exhibit lower fatigue resistance than conventionally processed (forged) materials. The fine LPBF microstructure in itself, can also influence the fatigue resistance, small grains and/or tiny solidification cells (around 1 µm size) favouring dislocations anchoring with a Hall-Petch-like effects, and a possible increase of yield strength and fatigue limit.

Compared with other as-built alloys (titanium based, nickel-based …), 316L stainless steel has been observed to reach outstanding mechanical monotonous properties, with an optimum balance between good ductility (usually more than 40 % elongation after LPBF), and elevated yield or ultimate strengths (respectively more than 550 MPa and 650 MPa) [8–10]. The explanation for such a behaviour is not fully achieved but could come from the fine microstructure, with typical inter-cell distances around 1 µm [11,12] combined with a high dislocation density (around 10^{15} m^{-2} [13]). In-depth analysis of the role of the dislocation network and nano-twinning during deformation of LPBFed 316L parts was done by Liu et. al [14]. Another important aspect to mention is that 316L is believed to be a rather defect-

tolerant material due to its high ductility that promotes a low notch sensitivity, as mentioned by Riemer et al [15].

Recent investigations have shown that post-LPBF surface processing of a 316L steel can significantly improve mechanical properties, especially in fatigue [16,17]. On the other hand, thermo-mechanical post processing such has HIP or high temperature heat treatments have proven to worsen the fatigue properties of 316L LPBF [15,18]. This was explained by the recrystallization phenomenon occurring at high temperature, and resulting in a strong reduction of dislocation density [19,20]. In that case, even if thermal or thermomechanical post-treatments reduce the dislocation density, they do not significantly increase the ductility (+10%) of the material, while reducing noticeably its yield strength (-30%) [18]. Heat treated materials will thus have relatively lower high cycle fatigue performances than as-built samples, for similar surface finish. In turn, according to Riemer et al. [15] and Leuders et al. [18], LPBF and machined 316L steel may be used without additional post-processing stages.

Considering various reported works on the fatigue behaviour of LPBF-ed 316L steel, a large scattering of fatigue limits at 10^6 cycles can be evidenced, for rather similar process conditions, but different surface finish. For instance, at R=-1 stress ratio, endurance limits vary between 200 MPa and 350 MPa [7,16,18,21], with a 200 MPa fatigue limit for as-built condition (Ra = 7 µm) versus 350 MPa after surface machining (Ra= 0.5 µm) [16]. This traduces the dominant effect of surface roughness even for a material usually considered as a defect tolerant material.

For low roughness, the sub-surface and internal defects will drive the fatigue performances. Zhang et al. [10] have evidenced that the fatigue properties of 316L fabricated in LPBF are impacted above 0.5 % of internal porosity, without discussing precisely the size threshold at which a defect can be impactful. Such high porosity thresholds tend to indicate that internal porosity in 316L parts will have a low impact on fatigue properties. However, the fatigue resistance of materials containing defects is mostly driven by their critical defects population. Apart from its shape and tortuosity, an unique critical defect (ie an artificially introduced defect that will drive and overcome all other possible fatigue failure mechanisms) will combine two major characteristics: a sufficient size and a reduced distance to the surface. Murakami's work in the field combined those two factors [22] by introducing a surface/internal defect

discrimination method, in addition to a higher harmfulness coefficient C for surface defects. The stress intensity factor calculated for a stress range $\Delta\sigma$ with a critical defect of size $\sqrt{Area}$ is given Eq. 1.

$$\Delta K = C * \Delta\sigma\sqrt{\pi\sqrt{Area}} \qquad \textit{Eq. 1}$$

A defect with radius r at a distance d between its center and the surface, is considered to be at the surface if the ratio r/d is over 0.8. The C coefficients 0.5 (internal defect) and 0.65 (surface defects) that are applied in the calculation of their respective stress intensity factors are equivalent to considering identical harmfulness between surface defects of a given size and 67% larger internal defects.

Romano et al. [23] and Le et al. [24] have both shown that it was possible to link different defect populations, with various statistical size distributions, to the fatigue properties of an AlSi10Mg and a Ti-6Al-4V alloy respectively. A correlation was also shown between stress intensity factors of the most detrimental defects detected by computed tomography and associated fatigue resistance.

Last, recent works by Andreau et al. [25] on LPBF-ed 316L have shown a systematic initiation of fatigue cracks on surface defects, despite the presence of 4 to 10 times larger internal defects in the bulk of small machined and polished cylindrical fatigue samples. Although those defects had a similar shape, only internal porosities of more than 400 µm equivalent diameter were shown to impact the fatigue properties. Another interesting result was the possibility to achieve high fatigue limits (500 MPa) at 10^6 cycles and R=0.1 stress ratio with totally free from defects samples.

Following this literature review, it appears that the two main factors that turn a defect into a critical defect for fatigue, need to be decorrelated in order to further analyse and model the respective fatigue strength sensitivity to each one of these parameters. Additionally, the need of more reference data for defect-free parts is also believed to be crucial in order to assess globally the fatigue performances of LPBF 316L parts.

In the current work, to facilitate the analysis of defects harmfulness, artificial pores were generated on purpose inside LPBF samples using the same early approach by Gong [26], and the same procedure

by Bonneric et al. [27]. In a first part, an optimization of defect shape was made, with the objective of obtaining as spherical as possible lacks-of-fusion with various submillimeter diameters and controlled distances from the surface. Then, fatigue tests were carried out to assess the influence of defect position and size. Corresponding results were compared with those obtained on fully optimized as-built LPBF 316L parts containing almost no porosity, and considered as a reference material. The global objective of the work was to characterize precisely the competition between surface and internal defects by creating parts containing deterministic defects.

2. Methods and tools

2.1. LPBF manufacturing of samples containing deterministic defects

The samples were manufactured using a SLM 125 HL machine (from SLM Solutions GmbH), which was equipped with a 400 W Nd:YAG gaussian laser and argon gas shielding, with less than 400 ppm O_2. The 316L powder feedstock used in this study is described elsewhere [2]. Optimized building parameters were determined by a parametric study [28] for a 30 µm layer thickness and a 73 µm (at $1/e^2$) spot diameter. Contour and hatching laser parameters are given in Table 1. A meander scanning strategy [29] was used to avoid any overlap between distinct parts that can induce pores [30,31]. A scan rotation after each layer was set at 33°. The forbidden scanning angles were set at ±45° versus the shielding gas direction to prevent the interaction between the laser and the vapor plume.

	Power (W)	**Scanning speed ($mm.s^{-1}$)**	**Hatch spacing or distance (µm)**	**Number of lines**
Hatching	200	800	110	/
Contour	100	400	70	2
Downskin hatching	100	1000	60	/
Downskin contour	100	1250	70	2

Table 1: Main laser parameter sets

Manufacturing deterministic spherical defects with LPBF requires a specific optimization step to ensure defects geometries as close as possible from CAD files. This is particularly important for the

contour parameters outlining the external defect shape. Contour parameters sets were thus used on both the outside (external contour) and the inside (internal contour) of the parts. (Figure 1 a)). Corresponding parameters are given in Table 1.

For all overhanging areas inclined by less than 59° from the X-Y plane, specific downskin parameter sets were applied. This low-energy parameter set (Table 1) replaces classic contour and hatching laser parameters, in order to minimize the energy (~ P/V) deposited by the laser in overhanging areas (Figure 1 b)). Favouring small melt pools in overhanging areas limits their collapse, and reduces the need for supporting [32–34], the absence of internal supports being mandatory for the spherical defects. For every overhang zone included in the downskin criterion, laser parameters of contour and hatching were shifted to their downskin equivalents for the next 5 layers (150 µm), according to the values given Table 1.

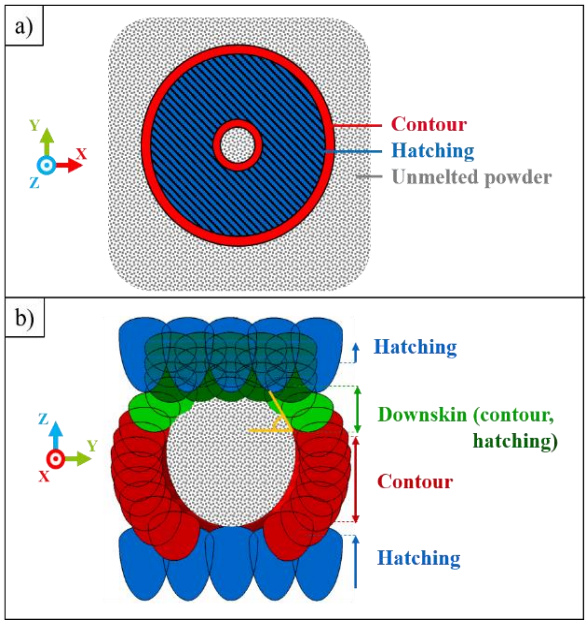

Figure 1: a) Laser scanning strategy used to melt the powder visualized in the X-Y plane b) Along the fabrication direction

2.2. Preparation of the fatigue samples

Two formats of fatigue samples have been manufactured. First, small fatigue samples (Figure 2 a)) were designed to minimise the probability (statistically) of a critical manufacturing defect, with a gauge volume of 48 mm^3. Second, larger fatigue samples (Figure 2 b)) were used to characterize the influence of internal deterministic defects (gauge volume: 283 mm^3). The large fatigue samples pertain to the ISO 1099:2017(E) norm. All the fatigue samples were obtained from LPBF square based blocks (small samples) or cylinders (large samples) manufactured vertically in the machine, after machining them to the required dimensions. The vertical manufacturing direction was chosen as to minimize the heterogeneities of the local applied stresses in the most loaded area of the deterministic defects, as the smoothness and symmetry of the manufactured defects was higher in the plane normal to the building direction. The machining step was chosen to reduce the as-built surface roughness that is known to impact the fatigue properties [16], from a Ra of 5-10 µm down to down to 0.1 µm after polishing. The machining residual stresses were then reduced with a 2 h thermal treatment at 350°C under argon atmosphere before furnace cooling.

A total of 7 optimized small samples (S-1 to S-7) were manufactured, as well as 24 large samples containing various deterministic defects. Among the large fatigue samples, 3 deterministic defect dimensions were chosen, along with 3 distances to the surface (Figure 2 c)). Their nomenclature and number are summarized on Table 2. The deterministic defect dimensions were chosen as to be larger than the grain size (typically comprised between 10 and 140 µm, as observed and detailed in previous work [25]), while being small enough to have a minimal impact on the stress distribution by reducing the total area of the gauge. Moreover, the deterministic defects of diameter 430 µm have a $\sqrt{area}$ of 380 µm, which is equal to the natural defect threshold size at which crack initiation occurred internally in previous work [25] for the same material (defect conglomerate visualized in Figure 5 d)). The various distances shown in Table 2 correspond to the length between the surface and the center of the defect. They correspond to a defect placed: (i) in the center of the sample, (ii) offcentered by a half of the gauge radius, (iii) at one defect diameter from the surface, and (iv) one radius from the surface (Figure 2 c)). The thinnest distance to the surface obtained was thus 215 µm, i.e. the radius of the middle sized

deterministic defect. A batch of 6 specimens with large section and without any deterministic defects were added to be used as a reference for large specimen and noted L-i.

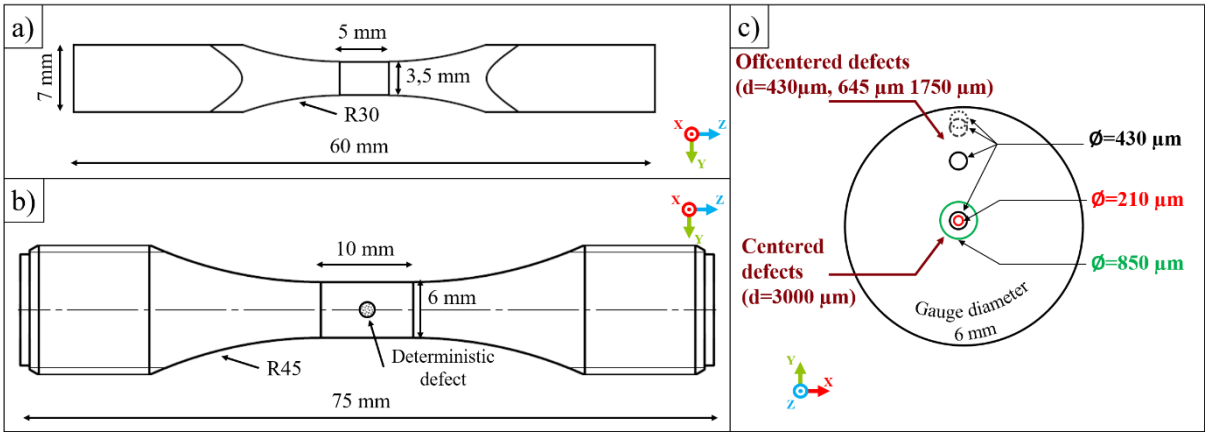

Figure 2: a) Small section samples, b) Large section samples (ISO 1099:2017(E)), c) Position and sizes of the deterministic defects in the large samples the size and position of the deterministic defects

Distance from defect center to surface	**Diameter**		
	210 µm	**430 µm**	**850 µm**
3000 µm (center)	C210-i (3)	C430-i (3)	C850-i (4)
1715 µm	/	M430-i (3)	/
645 µm	/	D430-i (3)	/
430 µm	/	R430-i (3)	/

Table 2: Nomenclature and number of the large samples depending on the size and position of the deterministic defects

2.3. Characterization tools

EBSD analysis was carried out on a Philips XL 40 Scanning Electron Microscope on polished cross sections, with a resolution of 1 µm per pixel. Additional EBSD parameters can be found in previous work [2].

µ-CT characterization was carried out on some dense samples and samples containing deterministic defects, with voxel sizes of 5x5x5µm^3 and 6.4x6.4x6.4 µm^3 respectively, by varying the

distance between the object and the detector. Defects with a volume inferior than 27 voxels were not considered. Additional µ-CT parameters can be found in previous work [25].

High cycle fatigue testings were carried out on small samples with a Rumul Testronic resonant machine with a load ratio R=0.1 at 65 Hz. The large samples were tested on a Zwick resonant machine at the same load ratio at a frequency of around 90 Hz. All samples were tested in air at ambient temperature, using the same step loading method, first described by Maxwell and Nicholas [35] and used in previous studies [25]. The method consisted in imposing a given stress level at each sample. If the sample did not fail before reaching 10^6 cycles, the maximum applied stress was increased by 20 MPa and the cycle count was reseted. The stop criterion (failure) was considered for the total failure of the sample, or a 1 Hz drop in the loading frequency. The difference in loading frequency between the two machines was considered to have a negligible impact on the fatigue properties. The fracture surfaces were analysed on a Zeiss EVO MA10 Scanning Electron Microscope in secondary electron mode.

3. Results

3.1. Microstructural and preliminary characterization

Some of the manufactured optimized samples were initially characterized by EBSD and metallography, in order to lay the microstructural environment of the study.

The observations showed partially elongated grains (Figure 3 a)) along the fabrication direction (Z axis), that are induced by epitaxial growth [36,37]. A grain shape anisotropy is evidenced by the smaller grain size (30 µm in equivalent diameter) in the plane perpendicular to the fabrication direction (X-Y plane) than in the plane parallel to the loading direction (50 µm) as seen in Figure 3 b) and c). A small texture (intensity ~3) can be observed with the preponderant [001] grain orientation (red color) along the X axis (Figure 3 a) and b)), in accordance with previous studies [2,9,38]. The numerous subgrain boundaries and the inhomogeneous colors in the grains are the result of a high dislocation density that accommodates crystallographic deformation, which is thought to be linked to the high

thermal gradients and rapid solidifications rates [39] of the LPBF process. Finally, a porosity analysis performed by tomography and metallography showed porosity rates of about 0.01%.

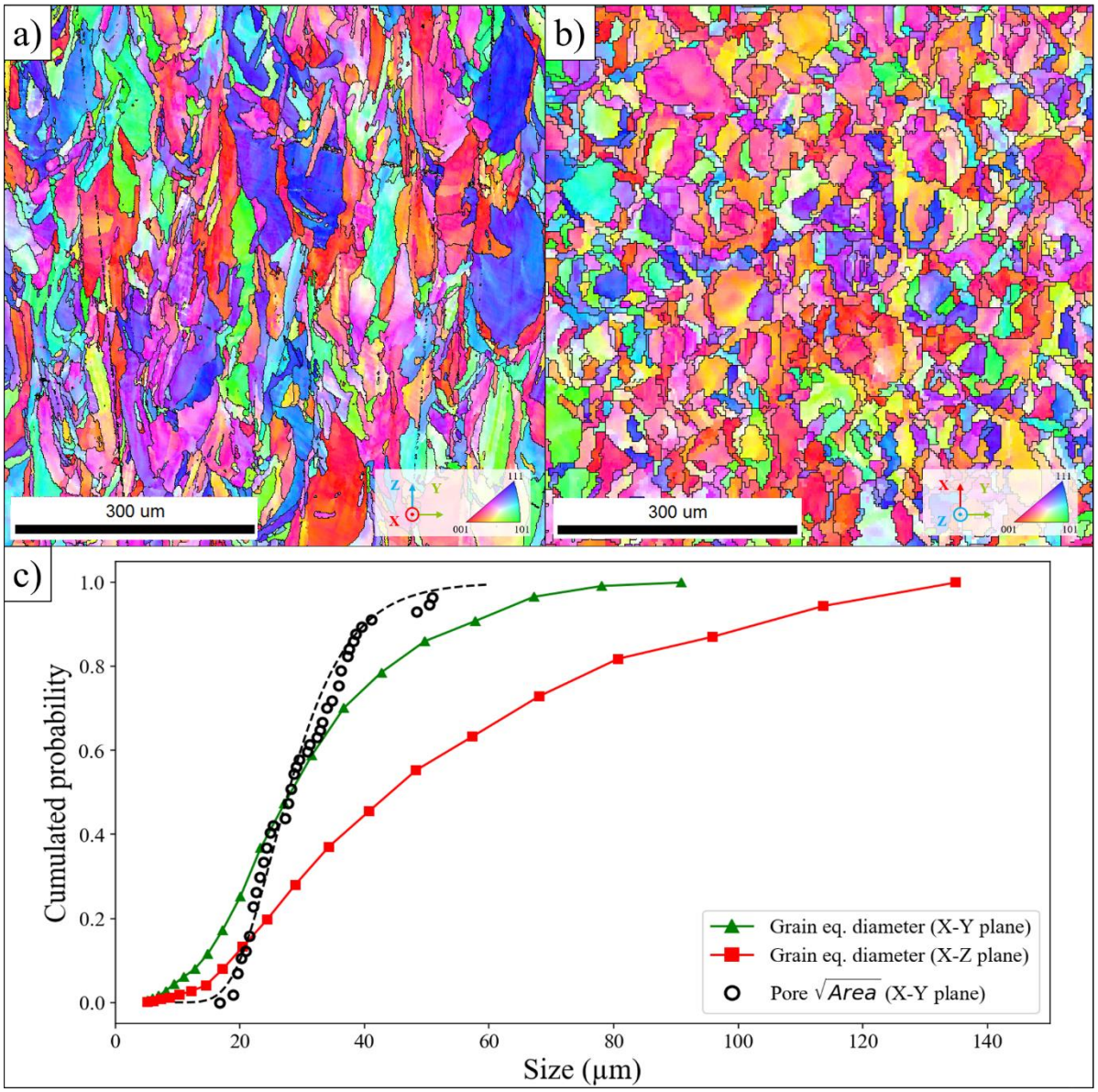

Figure 3: EBSD mapping of the microstructure visualized along the X axis and taken a) along the fabrication direction and b) on the plane perpendicular to the fabrication direction c) Comparison of the grain and pore size

In this work, the natural defect dimensions will be described using the common Murakami $\sqrt{area}$ parameter [22]. The defect population was measured in 70 mm^3 of material using X-ray tomography, and the parameters used can be found elsewhere [40]. The defect detection threshold was

set at 15 µm in $\sqrt{area}$. The volume was then subdivided in 30 subvolumes and the largest defect of each volume was measured, according to the Gumbel method [41], as in the work of Romano et al. [42]. The defect distribution showed that among the 405 pores detected, no pores with a root area superior than 50 µm were observed (Figure 3 c)). A finer 2D metallography analysis, with submicronic resolution, carried out on 144 mm² of polished X-Y cross sections, revealed that among the 1150 pores found, 97% had a $\sqrt{area}$ under 10 µm. Those manufacturing parameters sets were used in recent studies [40] and showed density rates over 99.99%.

Monotonic tensile test of heat relieved samples manufactured vertically using the hatching parameters sets of this study showed a 583±37 MPa maximum tensile strength, 448±32 MPa yield strength, with more 54±4% elongation [28]. Those results were in accordance with the common mechanical properties of LPBF 316L from literature [8,43,44]

3.2. Deterministic defect generation validation

In order to validate the method, a range of test deterministic pores were analysed with optical microscopy. Figure 4 a) reveals the various melt pools around an ovoid deterministic pore after etching and compares it to the 3D model. A non-sphericity on the upper part of the defect is evidenced by a melt-pool collapse, as well as a roughness increase, linked to the powder grains sticking. The microstructural analysis in EBSD (Figure 4 b)) reveals that the grain morphologies and sizes directly reflect the parameter sets used to manufacture the defects. The small grains on the top of the pore correspond to the downskin hatching parameter area realized with low volumetric energy. In this area, grains are smaller in size and more equiaxial than in the rest of the sample. As this area is located on the top of the pore, it was not believed to have an impact on the mechanical properties if a crack were to initiate on the largest pore section. The outline of the contour scan can also be observed around the deterministic defects, with slightly smaller grains than in a fully dense part. Indeed, due to the perpetual shifts in the laser scanning directions, the contour zones offer less opportunity for epitaxial growth than

the hatching zones. In addition, it was observed in previous work [25] that the grains usually grow perpendicularly to the scanning direction in the contour areas. A number of indents were realized in the hatching and in the contour zones and revealed $HV_{0.5}$ hardness values of 238±7 and 247±6 HV respectively. One can attribute this slightly higher hardness in the contour areas to the locally smaller grain size, via the Hall-Petch effect. This smaller grain size (<50 µm) is believed to be linked to the solidification conditions of the contour zones that are different from the bulk zones

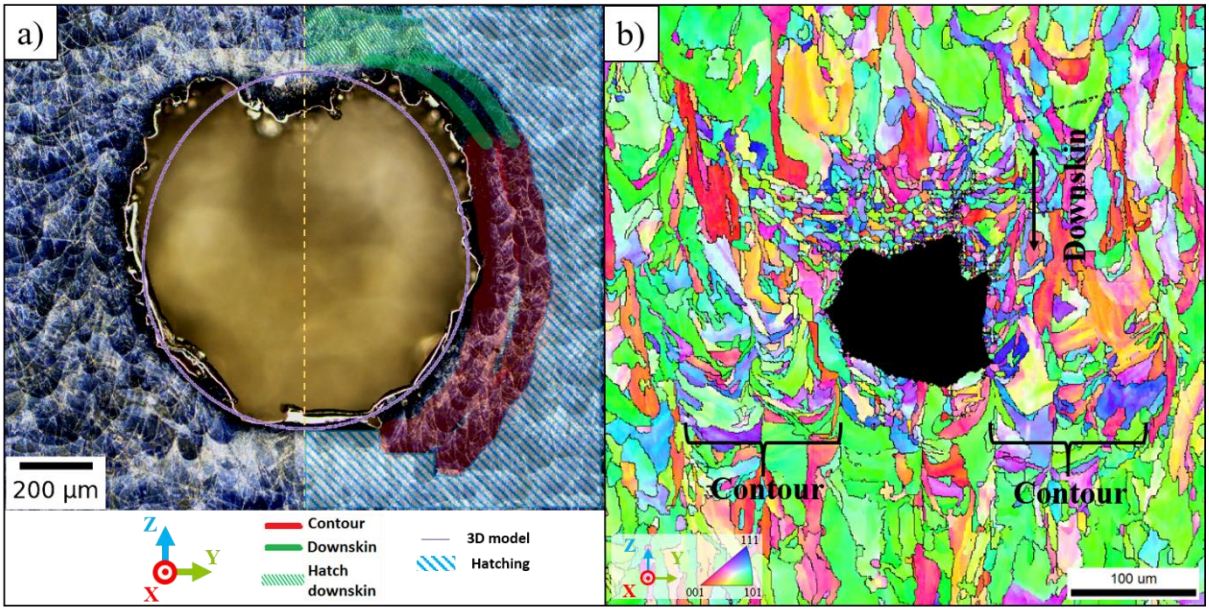

Figure 4: a) Melt pools and corresponding laser parameters sets around a test deterministic pore b) EBSD mapping around a small test deterministic pore according to the laser parameter sets, visualization along the Z-axis.

X-ray computed tomography observations were used for the 3D visualisation of the manufactured defects. The 3D reconstructions of deterministic defects (red) with target diameters of 900, 500 and 250 µm are shown in Figure 5 a) to c). The satellites pores (green) are much smaller than deterministic pores and were assumed to have a negligible impact on the mechanical properties. Those undesirable pores might have been be created by imperfect melt pool overlap in the contour areas, or instabilities in the melt pools in contour mode. The deterministic defects created with the method are highly symmetrical and must be considered as model defects. The natural lacks-of-fusion are much more

irregular and tortuous in shape (Figure 5 d)). However, as in natural lacks-of-fusion, the deterministic defects are filled with powder, as can been seen in the reconstruction in Figure 5 c). The mechanical contribution of the powder in the defects was considered negligible.

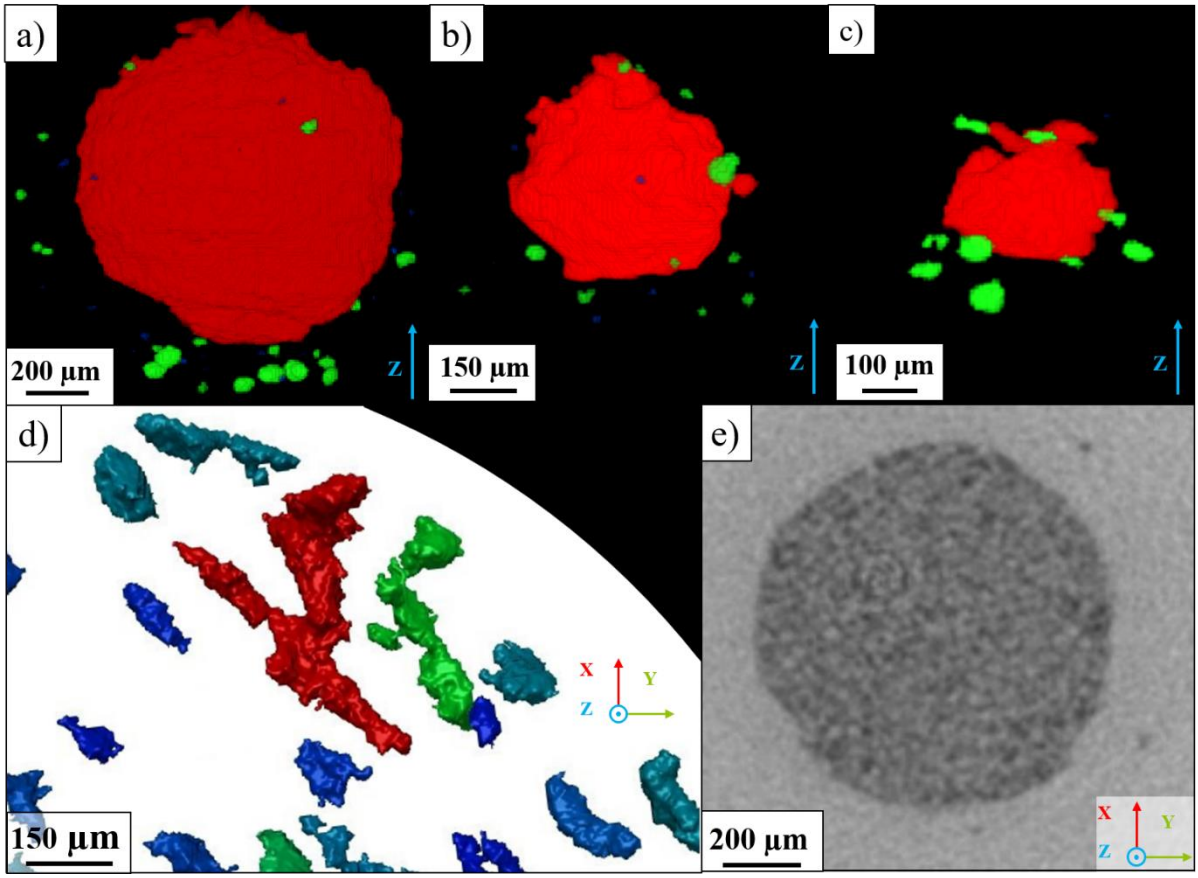

Figure 5: a) b) c) 3D reconstruction and colorization of deterministic pores of different sizes after µ-CT observation. d) Natural lacks-of-fusion observed in previous work [25] *e) Powder grains observed inside a deterministic pore.*

The deterministic defect generation method can be used successfully to create artificial pores of sizes in the range of 150 to 1000 µm, at any position in the bulk of a sample [28]. The variability in height and width were estimated at ±50 µm and ±20 µm for the largest pores. Defects with heights of 150 µm and less could not be manufactured repetitively, as their dimensions were too close from the powder dimensions (20-60 µm) and the melt pool dimension variability. As no internal crack initiation

was observed for natural defects measuring less than 300 µm [25], this defect generation method was considered sufficient to characterize realistically the impact of artificial defects.

3.3. Fatigue results

All the fatigue samples tested broke inside the gauge, after more than 1 step, except the sample R430-3. They were analysed post-mortem, in order to observe the crack initiation area. The sizes of the critical defects (natural or deterministic) were identified by their $\sqrt{area}$ in the X-Y plane, perpendicular to the loading direction. All the fatigue results are summarized in Table 3.

Sample	End step (MPa)	Number of steps	Cycles last step ($x10^5$)	√area defect (µm)	Critical defect
S-1	320	1	8.58	137	**Surface defect**
S-2	580	10	4.43	X	**Microstructure**
S-3	460	4	8.59	23	**Surface defect**
S-4	560	9	5.89	X	**Microstructure**
S-5	600	16	2.99	X	**Microstructure**
S-6	580	10	3.50	X	**Microstructure**
S-7	580	10	2.61	X	**Microstructure**
L-1	500	2	7.08	27	**Surface defect**
L-2	480	8	2.31	35	**Surface defect**
L-3	440	6	1.33	46	**Surface defect**
L-4	540	11	4.11	16	**Surface defect**
L-5	500	9	8.62	X	**Non observable**
L-6	520	10	3.66	42	**Surface defect**
C210-1	400	7	5.54	55	**Surface defect**
C210-2*	540	8	7.57	25	**Surface defect**
C210-3	520	8	5.46	31	**Surface defect**
C430-1	460	9	1.66	396	**Deterministic**
C430-2	480	10	3.85	388	**Deterministic**
C430-3	440	8	6.91	387	**Deterministic**
C850-1	380	1	3.98	832	**Deterministic**
C850-2	320	3	5.07	787	**Deterministic**
C850-3	340	4	2.10	819	**Deterministic**
C850-4	320	3	4.37	795	**Deterministic**
R430-1	440	6	5.54	425	**Deterministic**
R430-2	420	7	4.71	426	**Deterministic**
R430-3	440	8	/**	399	**Deterministic**
D430-1	420	5	6.75	403	**Deterministic**
D430-2	440	6	5.67	432	**Deterministic**
D430-3	440	8	4.28	408	**Deterministic**

M430-1	420	5	9.05	441	**Deterministic**
M430-2	460	7	2.64	439	**Deterministic**
M430-3	420	7	8.33	433	**Deterministic**

Table 3: Summary of all the fatigue tests carried out. 10^5 *cycles step instead of* 10^6 *cycles,* ** *failure during the first cycle of the last step*

3.1. Fatigue samples without deterministic defects

For all the specimens without artificial defect, crack did initiate from the surface. Among the optimized (small samples), two main failure origins were identified and corresponded to distinct groups in terms of fatigue performance. As indicated in Figure 6, samples S-1 and S-3 broke at stresses of 320 MPa (1 step) and 460 MPa (4 steps) respectively, whereas all the other samples survived for at least 9 steps and broke at a maximum stress of 560 MPa and above.

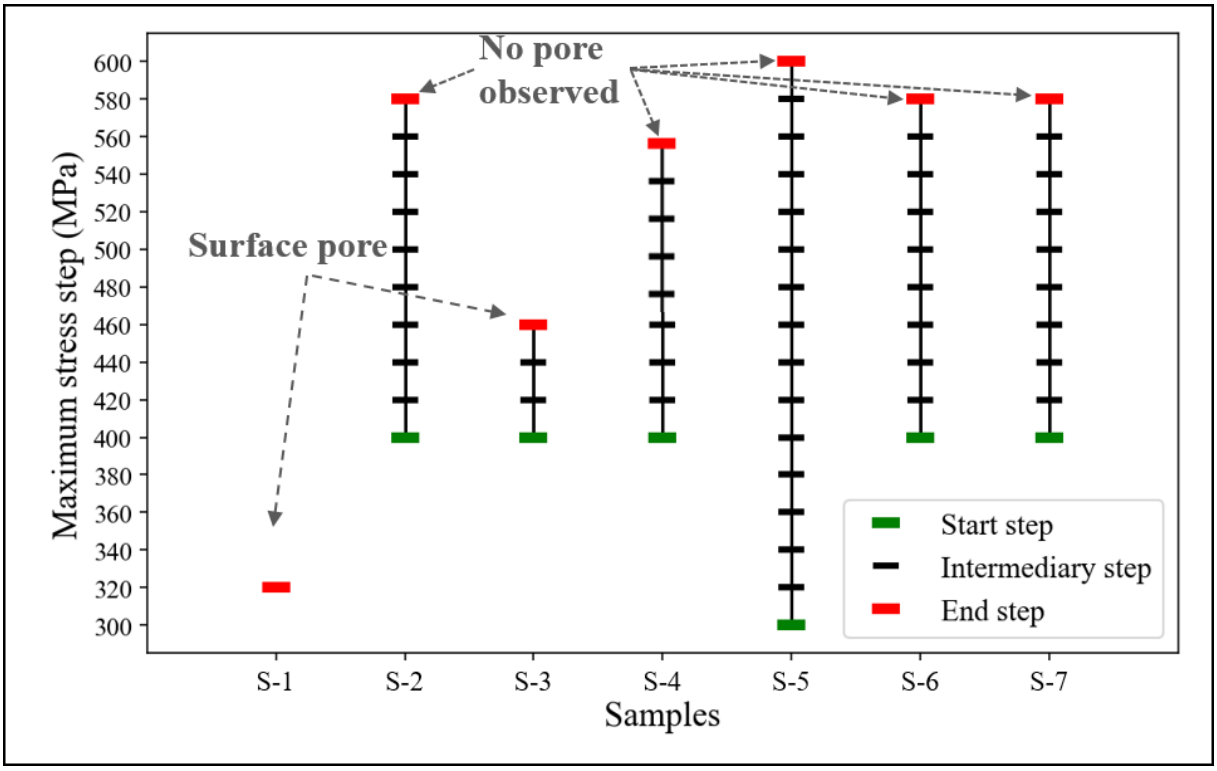

Figure 6: Stress steps applied using the Locati method for the optimized samples

The fracture surface analysis of samples S-1 and S-3 revealed that the cracks initiated on surface pores (Figure 7). Those pores were identified as lacks-of-fusion because of their irregular shape and the presence of ripples (Figure 7 b)), suggesting insufficient melt pool overlap. As the 137 µm defect was far larger than the observed pores in preliminary observations, it was considered to be an uncommon event of the manufacturing process. Its flatness along the Z direction could indicate a lack-of-fusion behind a large ejected particle, as observed in the literature [5]. The 23 µm defect was in the range of the usual defects root area in the bulk.

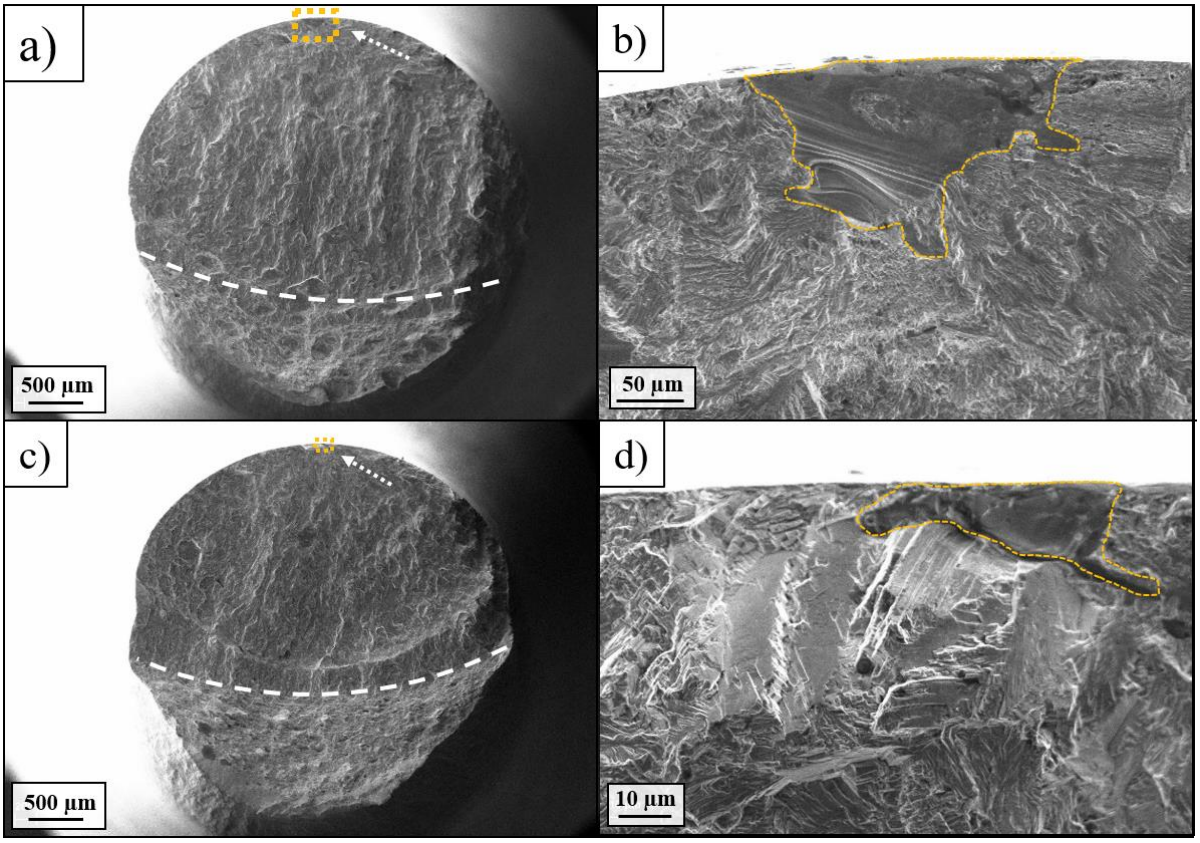

Figure 7: Fracture surface with enlarged image of the boxed critical defect for the sample a), b) S-1 and c), d) S-3. $\sqrt{area}$ of 137 and 23 µm respectively.

The other 5 samples (S 2, 4, 5, 6, 7) did not show any critical pores at the surface, or even internally. In that case, it is supposed that the crack initiation occurred due to microstructural effects, i.e. within a grain, a grain boundary, or an inter-cell boundary. Some evidence of shear facets with dimensions corresponding to the grain size can indeed be observed in Figure 8 a) and b) around the crack initiation zone. Other samples did not exhibit large sheared facets around the crack initiation zones, but exhibited fine and angular zones (Figure 8 c) to f)) whose geometry shows strong similitude with subgrain boundaries in LPBF samples [2]. Similar observations were made by Elangeswaran et al. [16], with no critical pores observed in the crack initiation areas. In their work, Zhang et al. [21] suggested the occurrence of crack branching around clustered oxide inclusions in 316 L LPBF fatigue loaded samples after HIP treatment. However, no trace of inclusions were found around the crack initiation zones in the S samples after elemental analysis.

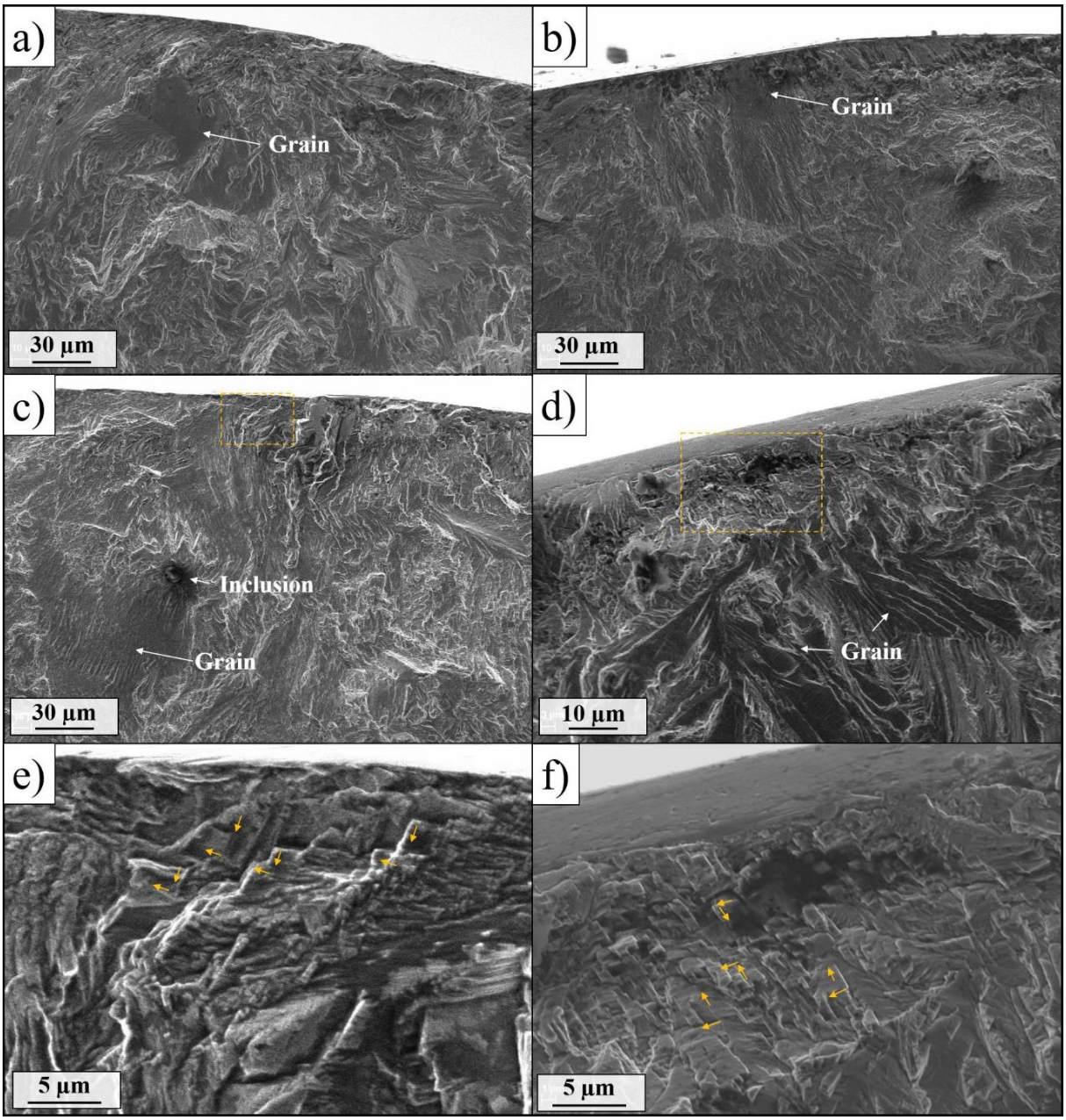

Figure 8: Crack initiation zones in a) S-6, b) S-5, c) S-4, d) S-7. e), f) Enlarged image in the boxed zones in c) and d) respectively

Among the large samples without artificial defects (L-1 to 6), crack initiation systematically occurred on measurable defects. All the critical defects were small in root area (<50 µm), with round shapes (Figure 9). An elemental analysis revealed the presence of silicon around some of those defects, suggesting the presence of inclusions already present in the feedstock [29]. In some cases, those defects can also be severely oxidized spatter generated during the manufacturing process and contaminating the

powder bed [45]. In both instances, improper melt pool wetting can occur on these particles, resulting in local stress-raisers like pores.

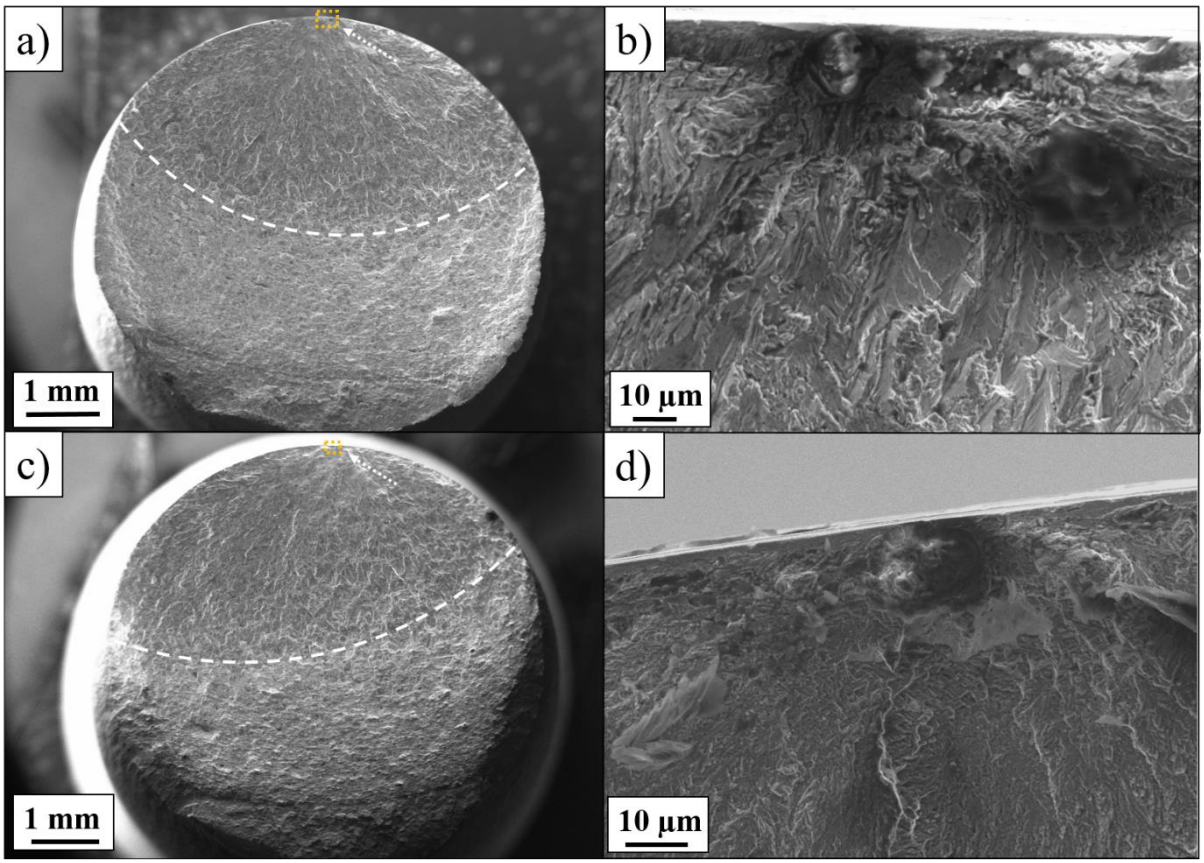

Figure 9: Fracture surface and close-up on the critical defect for a) b) Sample L-4 and c) d) Sample L-2

3.2. Fatigue samples containing deterministic defects

Among the samples with deterministic defects, the C210 set also showed cracks originating from accidental defects at the surface. Figure 10 a) and b) show that the crack initiation occurred on a lack of fusion defect, despite the presence of the much larger deterministic defect at the center of the fracture surface.

On the contrary, crack initiation always occurred on centered deterministic pores for the sets C430 and C850 (Figure 10 c) to f)), with larger dimensions (381 and 753 µm in $\sqrt{area}$ respectively), and no crack initiation was observed on the satellite pores. In those cases, the crack propagated all

around the deterministic defects, resulting in large *fisheye-like* fracture surfaces. It is likely that the crack initiation occurred in multiple areas around the deterministic pores, where the stress concentration is higher, and that all the micro cracks created connected during the propagation phase. This is suggested by the local crack initiation and propagation areas in the close up in Figure 10 g) and h), on the periphery of the deterministic pore. This observation is also sustained by the lines surrounding the large deterministic pore, that are positioned between local propagation zones, such as in Figure 10 g). These figures also evidence that the layer by layer construction of the internal defect induce roughness on the internal surface of the defect, that generate heterogeneous local stress concentrations that may promote multicrack inititation.

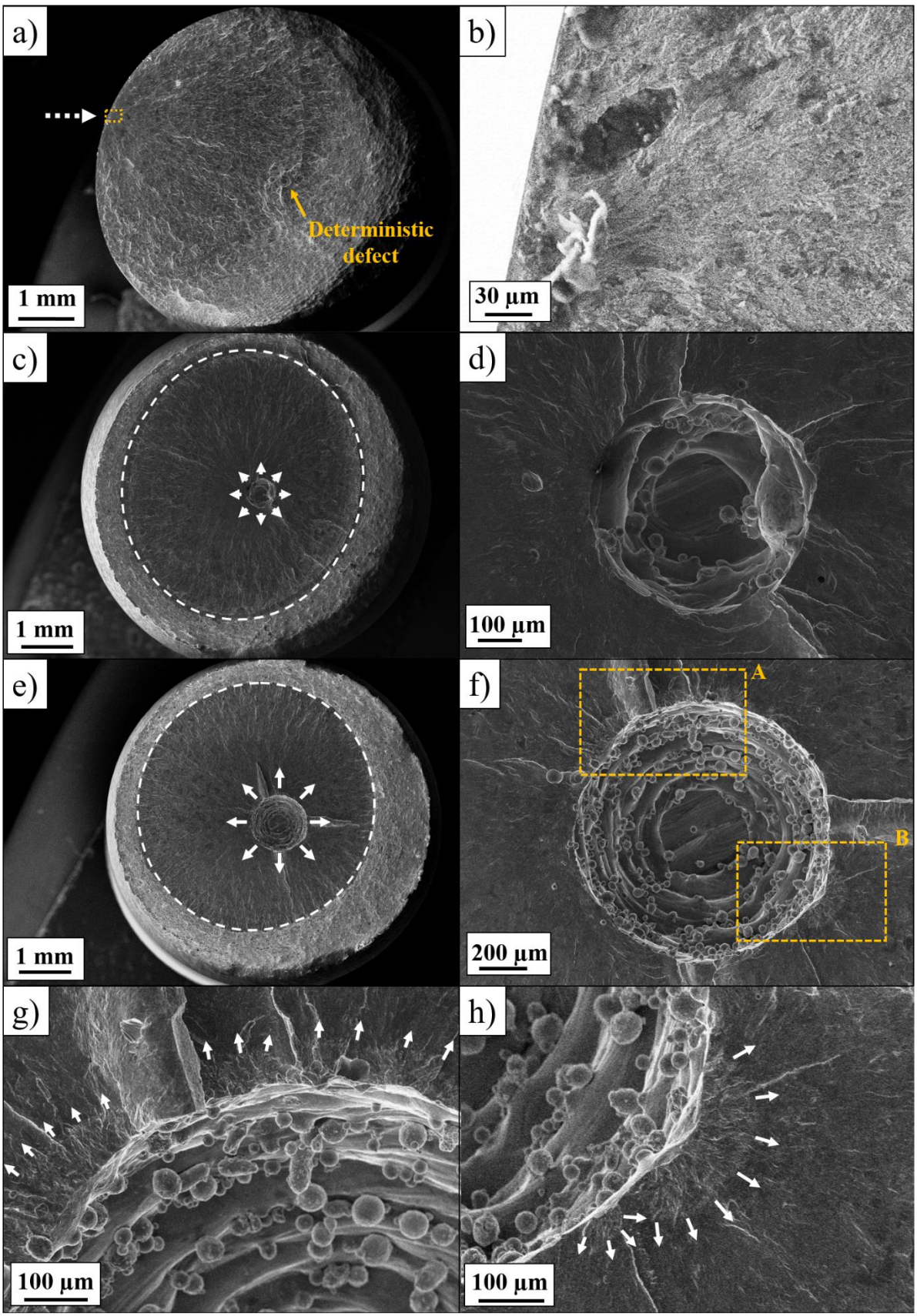
a)
Deterministic defect
1 mm
b)
30 µm
c)
1 mm
d)
100 µm
e)
1 mm
f)
A
B
200 µm
g)
100 µm
h)
100 µm

Figure 10: a) C210-1 fracture surface with b) close-up on the critical pore. c) C430-1 fracture surface with d) close-up on the critical (and deterministic) pore. e) C850-3 fracture surface with f) close-up on the critical (and deterministic) pore, g) h) close-up in f) in the boxed zones A and B respectively.

The three sample sets containing off-centered medium sized deterministic defects also showed a crack initiation occurring on the artificial defect (Figure 11 a) to c)). Most of the samples also exhibited a *fisheye-like* pattern, but some samples in R430 and D430 sets had highly asymmetric crack propagation (Figure 11 d)), contrarily to what could be expected from the literature [22]. This observation could be linked to the stress field distribution, where theoretical stresses are higher on the thin ligament side.

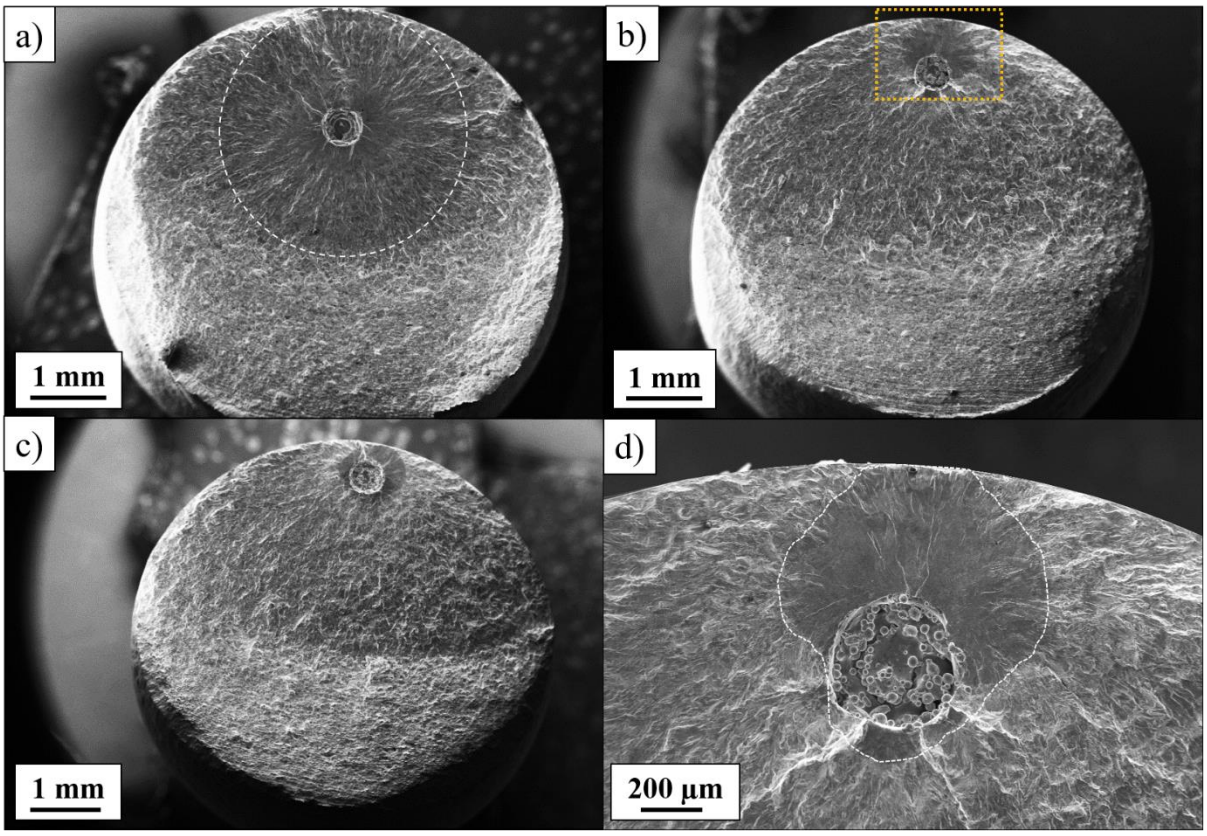

Figure 11: Fracture surfaces of samples a) M430-3, b) D430 -3 and c) R430-3. d) close-up picture on the deterministic pore in sample D430-3.

Performance-wise, no significant differences in fatigue endurance can be observed between the samples containing off-centered defects (R430, D430 and M430). In a similar manner, a centered defect

(C430 set) shows very little impact on the fatigue properties. Indeed, the Figure 12 only displays a 10% higher maximum stress at 10^6 cycles for the centered defects, but this observation could be offset by the high error bars. However, a noticeable performance increase can be noted when comparing with the internal natural defect from previous work (Figure 12). The very thin ligament size (110 µm) along with the tortuous shape of the natural defect (Figure 5 d)) could have impacted the fatigue properties.

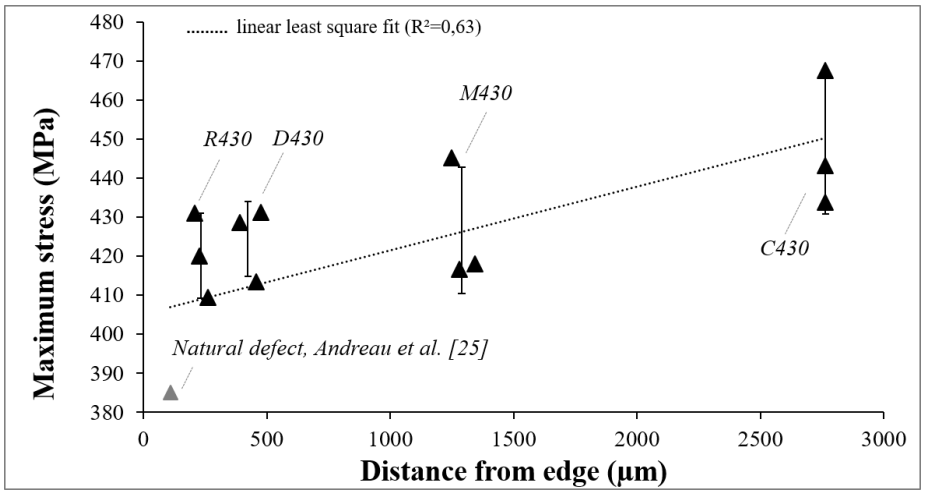

Figure 12: Evolution of the maximum stress with the distance between the defect and the surface of the sample

4. Discussion

All of the tests carried out in this study are reported in a Kitagawa diagram in Figure 13, along with the tests from previous work [25]. First, it must be emphasized that the fatigue endurance at 10^6 cycles obtained for the small optimal samples is extremely high in the absence of critical defects. To the knowledge of the authors, the average of 568 ±12 MPa found for the small samples where the crack initiated in the microstructure is the highest in the literature for 316L LPBF tested at R=0.1. Usual results for this material are in the 300-400 MPa range [10,46]. The extrapolation of the measurements performed by Elangeswaran et al. [16] on LPBF 316L at R=-1 to R=0.1 using the Gerber equation is however be extremely close (530 MPa fatigue limit at $2x10^6$ cycles). For 316L LPBF-HIP [21] or 316L

laminate [47] the uniaxial fatigue limits at 10^6 cycles and R=0.1 are usually around 360 MPa and 440 MPa respectively.

The very low fatigue strength variability (12 MPa) at 10^6 cycles in the absence of defect also indicates that the failure mechanisms involved in those 5 samples are likely to be identical. The authors indeed observed similar fracture surfaces and had a fairly low porosity rate in as-built samples. In the current study, the absence of critical defects was favoured by the optimized parameters, as well as a reduced gauge volume. The remaining defects were measured to be in the 10-50 µm range versus a typical grain size in the axial direction of 50 µm and larger grains above 100 µm. The common fatigue life theory by Murakami [22] shows that fatigue crack initiation requires the presence of a defect larger than a certain threshold, usually in the range of the grain size. It also states that surface defects are more deleterious. In the absence of significant surface defects, and with internal defects smaller than the grain size, the fatigue life will thus be controlled by the second most prevalent parameter: the microstructure. Advanced studies on the 316L LPBF microstructure [8,9] have shown that excellent strength-ductility combinations could be achieved, depending largely on the crystallographic orientation of the samples, and that it was even possible to surpass the properties obtained with conventional methods. Some results obtained by conventional methods extrapolated at R=0.1 [48] show lower fatigue performances, for identical failure mechanisms (microstructure crack initiation). In this study, the prevalent texture was oriented <011> along the loading direction, and comprised cellular sub-grains structures. This specific orientation, along with this fine microstructure, has been observed to accommodate very high deformations, by combining twinning and lattice rotation [9], in addition to some dislocation slip. It also raises the yield strength via a pseudo Hall-Petch effect [8], which is known to raise the fatigue life [49]. Those results are highly promising for metal additive manufacturing, by showing that the process not only enables higher part complexity, but could also make parts with highly improved fatigue endurance.

Despite parametric optimisation, numerous small pores remained in the samples. A fine 2D metallographic analysis revealed that 97% of those pores had $\sqrt{area}$ of 10 µm and under, and were thus not observed with X-ray tomography. However, no critical pore of 10 µm or less was ever observed in this study. Among the grains constituting the bulk, only 10% of them had dimensions of 10 µm and under (Figure 3 c)). This observation tends to suggest that the pores need to be larger than most of the surrounding grains to become critical, or else the fatigue life is primarily dictated by the microstructure, as it was observed for most of the optimized samples. Guerchais et al. [50,51] demonstrated this effect numerically by introducing defects with different sizes and shapes in artificial microstructures using polycrystalline plasticity coupled with probabilistic and deterministic fatigue models. In both cases they observed little impact of the defect on the endurance fatigue limit while the defect root area is below the grain size.

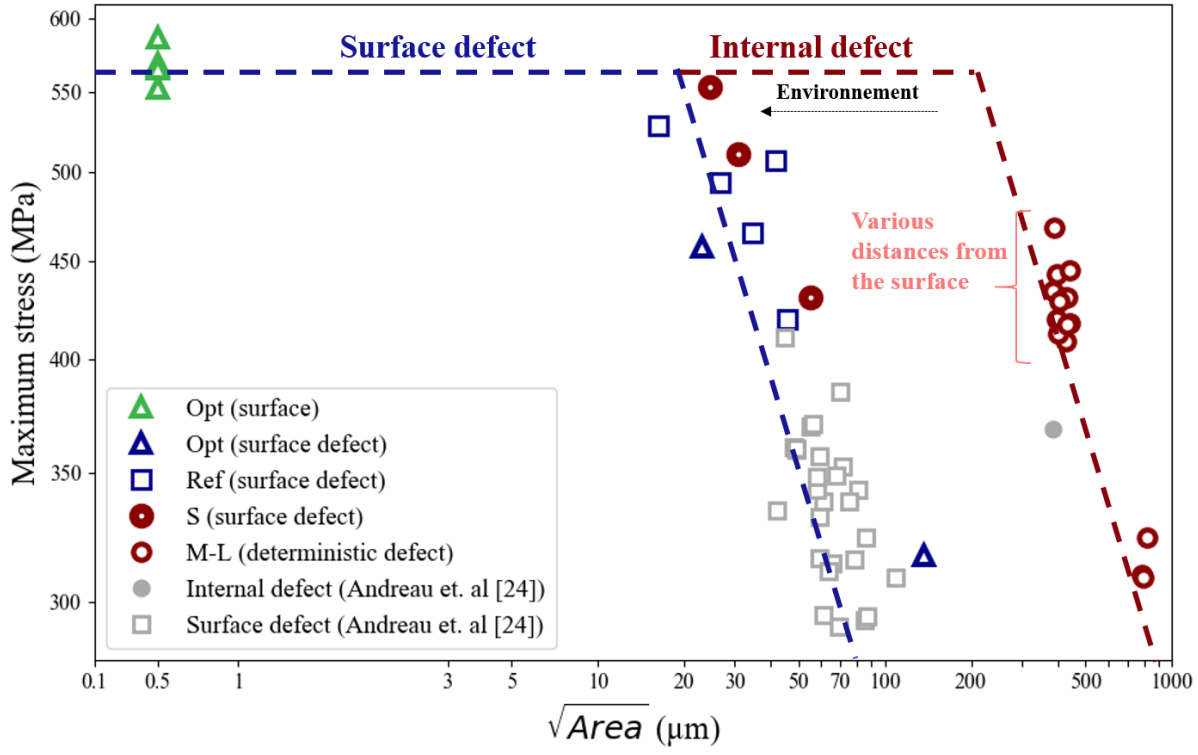

Figure 13: Kitagawa diagram for all the characterized samples. The defect size for the microstructural crack initiation was arbitrarily fixed at 0.5 µm (the range of the cell size).

It appears that the size threshold at which defects become critical depends mostly on their position: surface or bulk. These sizes measured in $\sqrt{area}$ are around 20 µm for surface defects, and at least ten times larger (200 µm) for internal defects. This result differs the Murakami criterion [22], which predicts that internal defects should compete with surface defects only 1.7 times larger. Indeed, in this study, artificial internal defects with a $\sqrt{area}$ of 186 µm (105 µm radius) were not critical for the fatigue life, and the critical crack initiation occurred on surface pores 3 to 7 times smaller. This experimental result confirms the early observations done in previous work [25] that suggested that internal defects in LPBF 316L are not critical, even with root areas 4 to 10 times larger than the surface defects dimensions. The distance from the surface at which internal defects become more deleterious has not been identified clearly in the current study, which suggest a low sensitivity of the material to the reduction of the ligament size. In particular, LPBF-ed 316L seems less impacted by subsurfacic defects than other LPBF-ed materials, such as an aluminium alloy studied by Bonneric et al. [27] under similar conditions. This observation is likely to be linked to the deformation tolerance of the material provided by its specific microstructure, and deformation mechanisms.

The slopes in the Kitagawa diagram in Figure 13: Kitagawa diagram for all the characterized samples. The defect size for the microstructural crack initiation was arbitrarily fixed at 0.5 µm (the range of the cell size). When an internal critical defect drives the fatigue properties, the dispersion of the measurements is low, which indicate that they are the primary factor influencing the fatigue endurance, before the microstructure. In turn, the stress concentration induced by the defects is likely to play a role. Indeed, the internal and critical lack-of-fusion characterized in previous work [25] but with the same $\sqrt{area}$ than 430 µm diameter deterministic defects limited the fatigue endurance to 370 MPa, versus 440 MPa in average with deterministic defects. The lacks-of-fusion cluster from previous work lacked symmetry and was highly tortuous, as illustrated in Figure 5 d). The stress concentration induced by its geometry remain however of second importance after its internal position. Indeed, it remains 7 to 8 times larger than the critical surface defects that induced identical fatigue performances.

Some indication as to why the critical pore dimensions are so far apart depending on their location could be found in the fracture surfaces. It can be observed in Figure 11 that the crack

propagation surfaces change completely when the crack is connected to the surface of the sample, going from flat to more striated. This change is particularly sharp when a defect is close to the surface, as in Figure 11 c) and d). The major difference that arises when the crack connects to the surface is the environnement. Indeed, the gas in the LPBF fabrication chamber is mostly argon (400 ppm of oxygen maximum). The gas surrounding the powder grains in deterministic pores is thus mostly argon, whereas air surrounds all the surface pores. Figure 14 a) and b) show close up pictures of a crack initiation and propagation occurring from a surface defect and an internal deterministic pore respectively. The rough crack path following surface pore crack initiation shows very few shared grains and consist mostly in intergranular propagation, while intragranular propagation is mostly observed for an internal pore crack initiation. Those observations are in accordance with several works on fatigue cracking in numerous alloys [53–55]. It is stated that air can weaken the grain boundaries, with the action of oxygen [56] or hydrogen [57]. The crack propagation could thus be highly impacted, as an intergranular crack propagation through fragilized grain boundaries becomes energetically favourable. On the opposite, argon has no action on the grain boundaries as it is inert, and samples behave like in vacuum.

However, no significant differences in fatigue life were observed between the R430, D430 and M430 sets, despite the cracks that benefited the inert argon atmosphere for various propagation length. Moreover, in the high cycle fatigue domain (around 10^6 cyles) the crack propagation time usually takes less than 10% of the total life of a fatigue sample [58]. One could still find differences in the early stages of propagation. As the deterministic defects are large, it could be expected that crack initiation occurs early, in multiple locations [59]. Only the most favourably oriented of those short cracks will propagate, through the easiest path [60,61]. The first microstructural barrier encountered by a short crack will thus play an important role. In argon, the beginning of intragranular crack propagation will require to shear the next grain the less favourably oriented, and pass over the barrier of the grain boundary (Figure 14 c)). However, with the help of air, intergranular crack propagation can occur at lower stress levels, as the crack will preferentially follow the weakened grain boundary. The stress level necessary to propagate a crack in argon atmosphere being higher than in air, it will require either a larger defect (higher stress concentration) or a higher stress level.

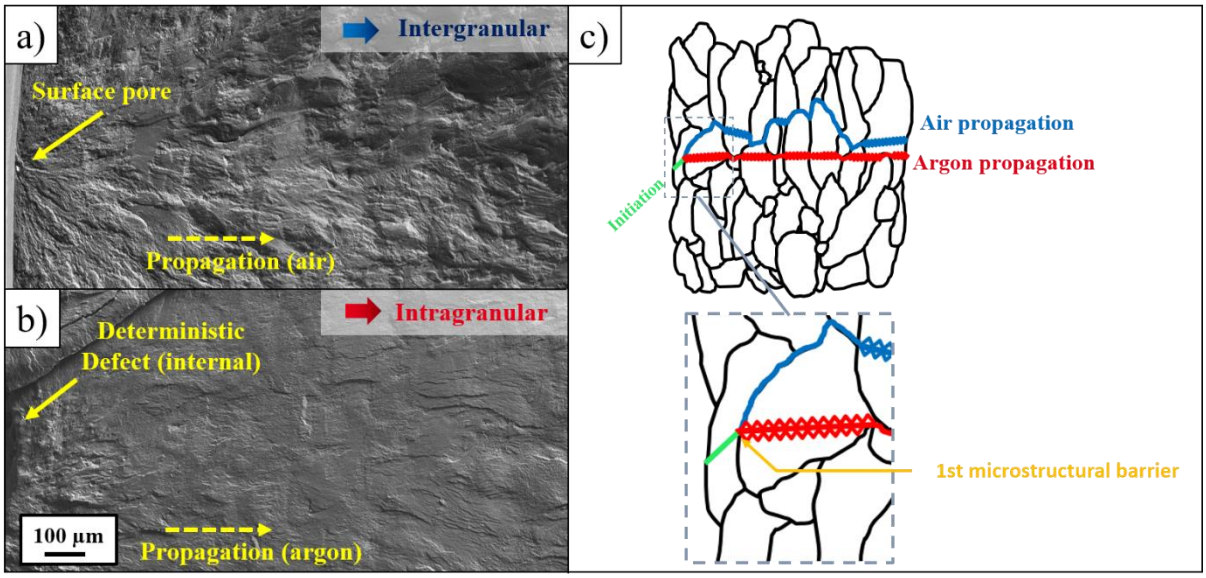

Figure 14: a), b) crack initiation and propagation zones for a surface and a deterministic internal pore respectively. c) Schematic illustration of the crack propagation in air and in argon.

For LPBF-ed 316L, a defect can be considered internal and thus be acceptable if it is located a few hundreds of microns under the surface, with dimensions not exceeding 200 microns approximatively. This result is of great importance, as it proves that obtaining a high density material up to roughly 300 µm under the surface, while maintaining an internal defect population with dimensions not exceeding 200 µm should provide excellent fatigue properties. The internal defect-tolerance of the LPBF-ed 316L could enable to speed up the manufacturing process with no impact on the fatigue properties. The productivity of the LPBF process is indeed one of the highest challenges in the industrial additive manufacturing world [1]. In a similar way, the defect control methods for LPBF-ed 316L should mainly focus on the subsurface, while a lesser resolution and quicker execution should suffice to detect internal deleterious defects.

5. Conclusions

316L fatigue samples have been manufactured using selective laser melting, using optimized parameters that offered a minimum amount of porosity. Thanks to the shape design freedom of the LPBF process, deterministic submillimetric round pores were generated in the bulk of the samples. Fully dense samples and other samples containing deterministic pores of various sizes and position were then tested in fatigue using a step method. Although the results of this study only apply to LPBF-ed 316L, the deterministic defect generation method could be used to characterize other alloys depending on their relative ductile or brittle behaviour. Several conclusions on the mechanical behaviour of LPBF-ed 316L can be drawn from this work:

- Fully optimized samples showed fatigue strength at 10^6 cycles very close to their maximum strength from tensile tests in the absence of critical pores, contrary to most other LPBF-ed alloys. Microstructural crack initiation was observed and the high mechanical properties can be linked to the fine microstructure of as-built LPBF-ed 316L samples.

- The dimensions at which a defect can become critical in fatigue depend mostly on its position. Surface pores were found to be far more deleterious than internal ones, with threshold root areas of around 20 µm versus 200 µm for pores under the sample surface. This observation confirms the trends observed in previous work that showed that large internal lacks-of-fusion were less deleterious than 4-10 times smaller surface defects.

- No significant differences were found in fatigue samples with 430 µm defects placed at various distances from the sample surface. Only a 10% increase in fatigue performance has been observed between offcentered and centered defect samples. It is suspected that defect tolerance of the LPBF-ed 316L is attributed to its high ductility, with multiple deformation accommodation mechanisms.

- Fracture surface analysis revealed that the gaseous environment in likely to play an important role on the fatigue life of the samples. As only inert gas surround internal pores, no embrittlement of the grain boundaries can occurs, contrary to surface pores surrounded by air. The first microstructural barrier before the crack propagation stage is considered to be the largest

obstacle to cross. Crack propagation from internal pores is mostly intragranular, which requires higher stress concentration than intergranular crack propagation from surface defects

Aknowledgements

This work was financially supported by the CEA List, the PIMM laboratory, the I2M laboratory and the LAMPA laboratory in France.

References

[1] T. Wohlers, Wohlers Report 2018. 3D Printing and Additive Manufacturing State of the Industry, 2018. doi:ISBN 978-0-9913332-2-6.

[2] O. Andreau, I. Koutiri, P. Peyre, J.-D. Penot, N. Saintier, E. Pessard, T. De Terris, C. Dupuy, T. Baudin, Texture control of 316L parts by modulation of the melt pool morphology in selective laser melting, J. Mater. Process. Technol. 264 (2019) 21–31. doi:10.1016/J.JMATPROTEC.2018.08.049.

[3] T. Niendorf, S. Leuders, A. Riemer, H.A. Richard, T. Tröster, D. Schwarze, Highly anisotropic steel processed by selective laser melting, Metall. Mater. Trans. B Process Metall. Mater. Process. Sci. 44 (2013) 794–796. doi:10.1007/s11663-013-9875-z.

[4] M. Colopi, A.G. Demir, L. Caprio, B. Previtali, Limits and solutions in processing pure Cu via selective laser melting using a high-power single-mode fiber laser, Int. J. Adv. Manuf. Technol. 104 (2019) 2473–2486. doi:10.1007/s00170-019-04015-3.

[5] G. Kasperovich, J. Haubrich, J. Gussone, G. Requena, Correlation between porosity and processing parameters in TiAl6V4 produced by selective laser melting, Mater. Des. 105 (2016) 160–170. doi:10.1016/j.matdes.2016.05.070.

[6] H. Wang, X. Zhang, G.B. Wang, J. Shen, G.Q. Zhang, Y.P. Li, M. Yan, Selective laser melting of the hard-to-weld IN738LC superalloy: Efforts to mitigate defects and the resultant microstructural and mechanical properties, J. Alloys Compd. 807 (2019). doi:10.1016/j.jallcom.2019.151662.

[7] T.M. Mower, M.J. Long, Mechanical behavior of additive manufactured, powder-bed laser-fused materials, Mater. Sci. Eng. A. 651 (2016) 198–213. doi:10.1016/j.msea.2015.10.068.

[8] Y.M. Wang, T. Voisin, J.T. McKeown, J. Ye, N.P. Calta, Z. Li, Z. Zeng, Y. Zhang, W. Chen, T.T. Roehling, R.T. Ott, M.K. Santala, P.J. Depond, M.J. Matthews, A. V. Hamza, T. Zhu, Additively manufactured hierarchical stainless steels with high strength and ductility, Nat. Mater. 17 (2018) 63–70. doi:10.1038/NMAT5021.

[9] X. Wang, J.A. Muñiz-Lerma, M. Attarian Shandiz, O. Sanchez-Mata, M. Brochu, Crystallographic-orientation-dependent tensile behaviours of stainless steel 316L fabricated by laser powder bed fusion, Mater. Sci. Eng. A. 766 (2019) 138395.

doi:10.1016/j.msea.2019.138395.

[10] M. Zhang, C.N. Sun, X. Zhang, P.C. Goh, J. Wei, D. Hardacre, H. Li, Fatigue and fracture behaviour of laser powder bed fusion stainless steel 316L: Influence of processing parameters, Mater. Sci. Eng. A. 703 (2017) 251–261. doi:10.1016/j.msea.2017.07.071.

[11] G. Marchese, M. Lorusso, S. Parizia, E. Bassini, J.W. Lee, F. Calignano, D. Manfredi, M. Terner, H.U. Hong, D. Ugues, M. Lombardi, S. Biamino, Influence of heat treatments on microstructure evolution and mechanical properties of Inconel 625 processed by laser powder bed fusion, Mater. Sci. Eng. A. 729 (2018) 64–75. doi:10.1016/j.msea.2018.05.044.

[12] C. Hardes, F. Pöhl, A. Röttger, M. Thiele, W. Theisen, C. Esen, Cavitation erosion resistance of 316L austenitic steel processed by selective laser melting (SLM), Addit. Manuf. 29 (2019) 100786. doi:10.1016/j.addma.2019.100786.

[13] S. Gorsse, C. Hutchinson, M. Gouné, R. Banerjee, Additive manufacturing of metals: a brief review of the characteristic microstructures and properties of steels, Ti-6Al-4V and high-entropy alloys, Sci. Technol. Adv. Mater. 18 (2017) 584–610. doi:10.1080/14686996.2017.1361305.

[14] L. Liu, Q. Ding, Y. Zhong, J. Zou, J. Wu, Y.L. Chiu, J. Li, Z. Zhang, Q. Yu, Z. Shen, Dislocation network in additive manufactured steel breaks strength–ductility trade-off, Mater. Today. 21 (2018) 354–361. doi:10.1016/j.mattod.2017.11.004.

[15] A. Riemer, S. Leuders, M. Thöne, H.A. Richard, T. Tröster, T. Niendorf, On the fatigue crack growth behavior in 316L stainless steel manufactured by selective laser melting, Eng. Fract. Mech. 120 (2014) 15–25. doi:10.1016/j.engfracmech.2014.03.008.

[16] C. Elangeswaran, A. Cutolo, G.K. Muralidharan, F. Berto, B. Van Hooreweder, C. Formanoir, K. Vanmeensel, Effect of post-treatments on the fatigue behaviour of 316L stainless steel manufactured by laser powder bed fusion, Int. J. Fatigue. 123 (2019) 31–39. doi:10.1016/j.ijfatigue.2019.01.013.

[17] R. Shrestha, J. Simsiriwong, N. Shamsaei, Fatigue behavior of additive manufactured 316L stainless steel parts: Effects of layer orientation and surface roughness, Addit. Manuf. 28 (2019) 23–38. doi:10.1016/j.addma.2019.04.011.

[18] S. Leuders, T. Lieneke, S. Lammers, T. Tröster, T. Niendorf, On the fatigue properties of metals manufactured by selective laser melting – The role of ductility, J. Mater. Res. 29 (2014) 1911–1919. doi:10.1557/jmr.2014.157.

[19] D. Kong, C. Dong, X. Ni, L. Zhang, J. Yao, C. Man, X. Cheng, K. Xiao, X. Li, Mechanical properties and corrosion behavior of selective laser melted 316L stainless steel after different heat treatment processes, J. Mater. Sci. Technol. 35 (2019) 1499–1507. doi:10.1016/j.jmst.2019.03.003.

[20] D. Kong, X. Ni, C. Dong, X. Lei, L. Zhang, C. Man, J. Yao, X. Cheng, X. Li, Bio-functional and anti-corrosive 3D printing 316L stainless steel fabricated by selective laser melting, Mater. Des. 152 (2018) 88–101. doi:10.1016/j.matdes.2018.04.058.

[21] M. Zhang, C. Sun, X. Zhang, J. Wei, D. Hardacre, H. Li, High cycle fatigue and ratcheting interaction of laser powder bed fusion stainless steel 316L : Fracture behaviour and stress-based modelling, Int. J. Fatigue. 121 (2019) 252–264. doi:10.1016/j.ijfatigue.2018.12.016.

[22] Y. Murakami, Metal Fatigue : Effect of Small Defects and Nonmetallic Inclusions, Elsevier, 2002.

[23] S. Romano, A. Brückner-foit, A. Brandão, J. Gumpinger, T. Ghidini, S. Beretta, Fatigue properties of AlSi10Mg obtained by additive manufacturing : Defect-based modelling and prediction of fatigue strength, Eng. Fract. Mech. 187 (2018) 165–189.

doi:10.1016/j.engfracmech.2017.11.002.

[24] V.D. Le, E. Pessard, F. Morel, F. Edy, Interpretation of the fatigue anisotropy of additively manufactured TA6V alloys via a fracture mechanics approach, Eng. Fract. Mech. 214 (2019) 410–426. doi:10.1016/j.engfracmech.2019.03.048.

[25] O. Andreau, E. Pessard, I. Koutiri, J.D. Penot, C. Dupuy, N. Saintier, P. Peyre, A competition between the contour and hatching zones on the high cycle fatigue behaviour of a 316L stainless steel: Analyzed using X-ray computed tomography, Mater. Sci. Eng. A. 757 (2019) 146–159. doi:10.1016/j.msea.2019.04.101.

[26] H. Gong, Generation And Detection Of Defects In Metallic Parts Fabricated By Selective Laser Melting And Electron Beam Melting And Their Effects On Mechanical Properties, Univ. Louisv. (2013). doi:10.18297/etd/515.

[27] M. Bonneric, C. Brugger, N. Saintier, Investigation of the sensitivity of the fatigue resistance to defect position in aluminium alloys obtained by Selective laser melting using arti fi cial defects, Int. J. Fatigue. 134 (2020) 105505. doi:10.1016/j.ijfatigue.2020.105505.

[28] O. Andreau, Nocivité en fatigue et contrôle de défauts produits par fabrication additive, HESAM, 2020. https://pastel.archives-ouvertes.fr/tel-02466522.

[29] R. Casati, J. Lemke, M. Vedani, Microstructure and Fracture Behavior of 316L Austenitic Stainless Steel Produced by Selective Laser Melting, J. Mater. Sci. Technol. 32 (2016) 738–744. doi:10.1016/j.jmst.2016.06.016.

[30] L.N. Carter, C. Martin, P.J. Withers, M.M. Attallah, The influence of the laser scan strategy on grain structure and cracking behaviour in SLM powder-bed fabricated nickel superalloy, J. Alloys Compd. 615 (2014) 338–347. doi:10.1016/j.jallcom.2014.06.172.

[31] S. Catchpole-Smith, N. Aboulkhair, L. Parry, C. Tuck, I.A. Ashcroft, A. Clare, Fractal scan strategies for selective laser melting of 'unweldable' nickel superalloys, Addit. Manuf. 15 (2017) 113–122. doi:10.1016/j.addma.2017.02.002.

[32] R. Mertens, S. Clijsters, K. Kempen, J.-P. Kruth, Optimization of Scan Strategies in Selective Laser Melting of Aluminum Parts With Downfacing Areas, J. Manuf. Sci. Eng. 136 (2014) 061012. doi:10.1115/1.4028620.

[33] H. Chen, D. Gu, J. Xiong, M. Xia, Improving additive manufacturing processability of hard-to-process overhanging structure by selective laser melting, J. Mater. Process. Technol. 250 (2017) 99–108. doi:10.1016/j.jmatprotec.2017.06.044.

[34] O. Andreau, P. Peyre, J.D. Penot, I. Koutiri, C. Dupuy, E. Pessard, N. Saintier, Deterministic defect generation in selective laser melting : parametric optimization and control, Lasers Manuf. - WLT EV. (2017) 1–11.

[35] D.C. Maxwell, T. Nicholas, A rapid method for generation of a Haigh Diagram for high cycle fatigue, in: T.L. Panotin, S.D. Sheppard (Eds.), 29, Fatigue an, 1999: pp. 626–641.

[36] L. Thijs, K. Kempen, J.P. Kruth, J. Van Humbeeck, Fine-structured aluminium products with controllable texture by selective laser melting of pre-alloyed AlSi10Mg powder, Acta Mater. 61 (2013) 1809–1819. doi:10.1016/j.actamat.2012.11.052.

[37] I. Yadroitsev, A. Gusarov, I. Yadroitsava, I. Smurov, Single track formation in selective laser melting of metal powders, J. Mater. Process. Technol. 210 (2010) 1624–1631. doi:10.1016/j.jmatprotec.2010.05.010.

[38] M. Shamsujjoha, S.R. Agnew, J.M. Fitz-Gerald, W.R. Moore, T.A. Newman, High Strength and Ductility of Additively Manufactured 316L Stainless Steel Explained, Metall. Mater. Trans. A Phys. Metall. Mater. Sci. 49 (2018) 3011–3027. doi:10.1007/s11661-018-4607-2.

[39] U. Scipioni Bertoli, B.E. MacDonald, J.M. Schoenung, Stability of cellular microstructure in laser powder bed fusion of 316L stainless steel, Mater. Sci. Eng. A. 739 (2019) 109–117. doi:10.1016/j.msea.2018.10.051.

[40] J. Liu, Y. Song, C. Chen, X. Wang, H. Li, C. Zhou, J. Wang, K. Guo, J. Sun, Effect of scanning speed on the microstructure and mechanical behavior of 316L stainless steel fabricated by selective laser melting, Mater. Des. 186 (2020). doi:10.1016/j.matdes.2019.108355.

[41] E.J. Gumbel, The Return Period of Flood Flows, Ann. Math. Stat. 12 (1941) 163–190. doi:10.1214/aoms/1177731747.

[42] S. Romano, A. Brandão, J. Gumpinger, M. Gschweitl, S. Beretta, Materials & Design Quali fi cation of AM parts : Extreme value statistics applied to tomographic measurements, 131 (2017) 32–48. doi:10.1016/j.matdes.2017.05.091.

[43] M.S. Pham, B. Dovgyy, P.A. Hooper, Twinning induced plasticity in austenitic stainless steel 316L made by additive manufacturing, Mater. Sci. Eng. A. 704 (2017) 102–111. doi:10.1016/j.msea.2017.07.082.

[44] M.L. Montero-Sistiaga, M. Godino-Martinez, K. Boschmans, J.P. Kruth, J. Van Humbeeck, K. Vanmeensel, Microstructure evolution of 316L produced by HP-SLM (high power selective laser melting), Addit. Manuf. 23 (2018) 402–410. doi:10.1016/j.addma.2018.08.028.

[45] V. Gunenthiram, P. Peyre, M. Schneider, M. Dal, F. Coste, I. Koutiri, R. Fabbro, Experimental analysis of spatter generation and melt-pool behavior during the powder bed laser beam melting process, J. Mater. Process. Technol. 251 (2018) 376–386. doi:10.1016/j.jmatprotec.2017.08.012.

[46] A.B. Spierings, T.L. Starr, I. Ag, Fatigue performance of additive manufactured metallic parts, 2 (2013) 88–94. doi:10.1108/13552541311302932.

[47] K.A. Mohammad, E.S. Zainudin, S.M. Sapuan, N.I. Zahari, A. Aidy, Fatigue Life for Type 316L Stainless Steel under Cyclic Loading, Adv. Mater. Res. 701 (2013) 77–81. doi:10.4028/www.scientific.net/amr.701.77.

[48] R. Guerchais, F. Morel, N. Saintier, The effect of the microstructure and defects on crack initiation in 316L stainless steel under multiaxial high cycle fatigue, Adv. Mater. Res. 891–892 (2014) 815–820. doi:10.4028/www.scientific.net/AMR.891-892.815.

[49] B. Gerin, E. Pessard, F. Morel, C. Verdu, A. Mary, Beneficial effect of prestrain due to cold extrusion on the multiaxial fatigue strength of a 27MnCr5 steel, Int. J. Fatigue. 92 (2016) 345–359. doi:10.1016/j.ijfatigue.2016.07.012.

[50] R. Guerchais, N. Saintier, F. Morel, C. Robert, Micromechanical investigation of the influence of defects in high cycle fatigue, Int. J. Fatigue. 67 (2014) 159–172. doi:10.1016/j.ijfatigue.2014.01.005.

[51] R. Guerchais, F. Morel, N. Saintier, Effect of defect size and shape on the high-cycle fatigue behavior, Int. J. Fatigue. 100 (2017) 530–539. doi:10.1016/j.ijfatigue.2016.12.010.

[52] A.A. Griffith, The phenomena of rupture and flow in solids, Philos. Trans. R. Soc. London. Ser. A. 221 (1921). doi:10.1098/rsta.1921.0006.

[53] J. Petit, J. de Fouquet, G. Henaff, Influence of ambient atmosphere on fatigue crack growth behaviour of metals, in: Handb. Fatigue Crack Propag. Met. Struct., 2012: pp. 1159–1203. doi:10.1016/b978-0-444-81645-0.50010-x.

[54] N. Grindberg, The effect of vacuum on fatigue crack growth, Int. J. Fatigue. (1982) 83–95. doi:https://doi.org/10.1016/0142-1123(82)90064-0.

[55] W. R.J.H, Fractography of Fatigue Crack Propagation in 2024-T3 and 7075-T6 Aluminum Alloys in Air and Vacuum, Metall. Trans. A. 6 (1975) 1587–1596. doi:10.1007/BF02641972.

[56] D. Duquette, M. Gell, The effect of environment on the mechanism of stage 1 fatigue fracture, Metall. Trans. Vol.2(5) (1971) Pp.1325-1331.

[57] T. Kanezaki, C. Narazaki, Y. Mine, S. Matsuoka, Y. Murakami, Effects of hydrogen on fatigue crack growth behavior of austenitic stainless steels, Int. J. Hydrogen Energy. 33 (2008) 2604–2619. doi:10.1016/j.ijhydene.2008.02.067.

[58] D. Socie, Critical Plane Approaches for Multiaxial Fatigue Damage Assessment, in: Adv. Multiaxial Fatigue, ASTM International, 100 Barr Harbor Drive, PO Box C700, West Conshohocken, PA 19428-2959, n.d.: pp. 7-7–30. doi:10.1520/STP24793S.

[59] F. Morel, N. Huyen, Plasticity and damage heterogeneity in fatigue, Theor. Appl. Fract. Mech. 49 (2008) 98–127. doi:10.1016/j.tafmec.2007.10.006.

[60] E.R. De Los Rios, Z. Tang, K.J. Miller, Short Crack Fatigue Behaviour in a Medium Carbon Steel, Fatigue Fract. Eng. Mater. Struct. 7 (1984) 97–108. doi:10.1111/j.1460-2695.1984.tb00408.x.

[61] E.R. De Los Rios, H.J. Mohamed, K.J. Miller, a Micro-Mechanics Analysis for Short Fatigue Crack Growth, Fatigue Fract. Eng. Mater. Struct. 8 (1985) 49–63. doi:10.1111/j.1460-2695.1985.tb00419.x.